# Vigorous lateral export of the meltwater outflow from beneath an Antarctic ice shelf

**Alberto C. Naveira Garabato**[1], **Alexander Forryan**[1], **Pierre Dutrieux**[2,3], **Liam Brannigan**[4], **Louise C. Biddle**[5], **Karen J. Heywood**[5], **Adrian Jenkins**[2], **Yvonne L. Firing**[6] **and Satoshi Kimura**[2]

**Affiliations**

[1]Ocean and Earth Science, University of Southampton, National Oceanography Centre, Southampton, SO14 3ZH, UK.

[2]British Antarctic Survey, Cambridge, CB3 0ET, UK.

[3]Lamont-Doherty Earth Observatory of Columbia University, Palisades, NY 10964, USA.

[4]Department of Meteorology, Stockholm University, Stockholm, SE-106 91, Sweden

[5]Centre for Ocean and Atmospheric Sciences, School of Environmental Sciences, University of East Anglia, Norwich, NR4 7TJ, UK.

[6]National Oceanography Centre, Southampton, SO14 3ZH, UK.

*__Corresponding author: acng@noc.soton.ac.uk__

**Instability and accelerated melting of the Antarctic Ice Sheet are one of the foremost elements of contemporary global climate change[1,2]. Increased freshwater output from Antarctica is regularly highlighted as a significant player in determining sea level rise[1,3], the fate of Antarctic sea ice and its effect on the Earth's albedo[4,5], on-going changes in global deep-ocean ventilation[3,6], and the evolution of Southern Ocean ecosystems and carbon cycling[7,8]. A key uncertainty in assessing and predicting the impacts of Antarctic ice sheet melting concerns the vertical distribution of the exported meltwater. This is commonly represented by climate-scale models[3-5,9] as a near-surface freshwater input to the ocean, yet measurements around Antarctica reveal the meltwater to be concentrated at deeper levels[10-14]. Here, we use observations of the turbulent**

**properties of the meltwater outflows from beneath a rapidly-melting Antarctic ice shelf to identify the mechanism responsible for the meltwater's deep focus. We show that the initial ascent of the meltwater outflow from the ice shelf cavity triggers centrifugal instability, which promotes vigorous lateral export, rapid dilution by turbulent mixing, and the ultimate settling of meltwater at depth. The relevance of this mechanism to a broad spectrum of Antarctic ice shelves is substantiated with an idealised ocean circulation model. Our findings demonstrate that the widely documented presence of meltwater at depth is a dynamically robust feature of Antarctic melting, and call for the representation of its underpinning mechanism in climate-scale models.**

The ice shelves of West Antarctica are losing mass at accelerated rates[2,15], possibly heralding the instability and future collapse of a significant sector of the Antarctic Ice Sheet[16]. The recent rapid thinning of the ice shelves is generally attributed to basal melt driven by warm sub-surface waters originating in the mid-latitude Southern Ocean[17,18], and the mechanisms responsible for the enhanced oceanic delivery of heat to the ice shelves are beginning to be understood[19,20]. In contrast, comparatively little is known about the pathways and fate of the increasing amounts of meltwater pouring into the ocean from the ice shelves. While a widespread freshening of the polar seas fringing Antarctica has been documented over the period of elevated ice shelf mass loss[3,21], the processes regulating the export of meltwater from the ice shelves remain undetermined, with a key focus of debate being the vertical distribution of the exported meltwater[22]. Ice shelf melting is characterised as a surface freshwater source by many climate-scale models[3-5,9], yet this representation appears at odds with the common observation of meltwater being concentrated in the thermocline (at depths of several hundred metres) across the Antarctic polar seas[10-14].

To resolve this conundrum, we conducted a set of detailed measurements of the hydrographic, velocity and shear microstructure properties of the flow in the close vicinity of the calving front of Pine Island Ice Shelf (PIIS; Fig. 1), one of the fastest-melting ice shelves in Antarctica[15,17]. The observations were obtained in 12 – 15 February 2014 from the *RRS James Clark Ross* under the auspices of the U.K.'s Ice Sheet Stability programme (iSTAR), and were embedded within a cyclonic gyre circulation spanning Pine Island Bay (Fig. 1). This gyre conveys relatively warm Circumpolar Deep Water toward the ice shelf cavity in its northern limb, and exports meltwater-rich glacially-modified water (GMW) away from the cavity in its southern limb[10,23]. Our measurements included sections of 140 hydrographic and 70 microstructure profiles with respective horizontal spacings of ~0.3 km and ~0.6 km, directed either parallel to the entire PIIS calving front at a horizontal distance of 0.5 – 1 km (transects S1A – S1B, Fig.1) or perpendicular to the calving front along the main GMW outflow from the cavity (transect S2, Fig. 1). Further details of the data set are given in the Methods. As regional tidal flows are weak, aliasing of tidal variability by our observations is insignificant to our analysis (see Supp. Info.).

An overview of the observed circulation across the PIIS calving front is provided by Fig. 2. Circumpolar Deep Water warmer than 0°C enters the ice shelf cavity beneath the thermocline, centred at a depth of 400 – 500 m (Fig. 2a). Colder Winter Water occupies the upper ocean, and acquires its near-freezing temperature from the strong oceanic heat loss to the atmosphere that occurs in Pine Island Bay throughout much of the year[24]. The layer of Winter Water is punctuated by a series of warmer (>0.8°C), 1 – 3 km-wide lenses in the 200 – 400 m depth range that are associated with rapid flow out of the cavity (Fig. 2b) and contain meltwater-rich GMW (Fig. 2c). GMW is warmer than the surrounding Winter Water because it has properties intermediate between the Circumpolar Deep Water and meltwater from which it derives[10]. Although GMW outflows the cavity at several locations, its export is focussed on a fast, narrow jet at the southwestern end of the PIIS calving front, where cross-front speed surpasses 0.5 m $s^{-1}$. Outflowing lenses of GMW are consistently characterised by very intense small-scale turbulence, with rates of turbulent kinetic energy dissipation ($\varepsilon \sim 10^{-7}$ W $kg^{-1}$) and diapycnal mixing ($\kappa \sim 10^{-2}$ $m^2$ $s^{-1}$) exceeding oceanic background values by typically three orders of magnitude (Figs. 2c,d; see Supp. Info.). This vigorous turbulent mixing promotes the rapid dilution and dispersal of GMW, and opposes the ascent of the exported meltwater to the upper ocean as a coherent flow.

The cause of the strong turbulence affecting the GMW outflows is unveiled by the observations along transect S2 (Fig. 3), directed normal to the PIIS calving front and approximately following the main GMW export pathway (Fig. 1). The warm signature of GMW extends laterally within the 200 – 400 m depth range and up to ~2 km away from the calving front, contained within a density class (27.7 – 27.8 kg $m^{-3}$) that is stretched vertically relative to offshore conditions (Fig. 3a). This main lens of GMW is connected to a thin filamentary feature with a vertical scale of a few tens of metres that penetrates to ~4 km off the calving front, and that is surrounded by layers of Winter Water. The suggested pattern of three-layered overturning flow is quantitatively endorsed by the measured horizontal and vertical components of velocity (Figs. 3b-c). These show GMW flowing northwestward (i.e. offshore) at ~0.3 m $s^{-1}$ and upward at ~0.01 m $s^{-1}$, consistent with the predominantly lateral circulation and vertical stretching inferred from hydrographic properties. The layers of Winter Water are seen to flow slowly southeastward (i.e. onshore) and downward at rates of ~0.01 m $s^{-1}$, indicating a role in replenishing the areas near the calving front from which GMW is exported. The GMW's edges are characterised by large horizontal shear (Fig. 3b), abrupt reversals in the direction of vertical motion (Fig. 3c), and greatly elevated rates of turbulent dissipation (Fig. 3d). This suggests that the primarily lateral flow and intense turbulent mixing experienced by GMW, which determine the meltwater's ultimate settling at depth after leaving the ice shelf cavity, are underpinned by the same ocean dynamics.

To elucidate these dynamics, the susceptibility of the circulation to overturning instabilities in the region of the main GMW export pathway is assessed by examining the distribution of potential vorticity ($q$) along transect S2 (Fig. 3e). The procedures for this and subsequent calculations are described in the Methods. A variety of overturning instabilities may develop in a geophysical fluid when $q$ takes the opposite sign to the planetary vorticity[25,26], which is negative in the Southern Hemisphere. These instabilities induce an overturning circulation that extracts energy from the background flow and expends it in the production of small-scale turbulence, mixing the fluid toward a state of marginal stability. The bulk of the transect is characterised by negative values of $q$ on the order of $-1 \times 10^{-9}$ $s^{-3}$, indicative of stable conditions. However, substantial patches of positive $q$ approaching or exceeding $1 \times 10^{-9}$ $s^{-3}$ are also present, notably along the upper and offshore edges of the main lens of GMW and near the terminus of the thin GMW filament. The fulfilment of the instability criterion in these areas suggests that the overturning circulation (Figs. 3b-c) and intense turbulence (Fig. 3d) revealed by our measurements arise from instability of the GMW flow exiting the PIIS cavity.

Overturning instabilities are respectively termed gravitational, symmetric or centrifugal if the fluid's vertical stratification, horizontal stratification or relative vorticity is responsible for meeting the instability criterion, in which case instabilities extract energy from the available potential energy, vertical shear or lateral shear of the background flow[26,27]. The nature of the instability experienced by the GMW outflow is evaluated in two ways. First, the relative importance of the three above factors contributing to the instability criterion is quantified via a balanced Richardson angle analysis[27] of the transect S2 data (see Methods). This indicates that the GMW outflow is primarily subject to centrifugal instability (Fig. 3e, contours), triggered by the large anticyclonic relative vorticity that characterises the outflow (see Supp. Info.). Symmetric instability also affects the offshore edge of the main lens of GMW, where significant horizontal stratification occurs as a result of the lens' vertical stretching (Fig. 3a). Second, the energy sources of the three instability types are estimated from the same data set (see Methods), and the extent to which they balance the observed turbulent dissipation is assessed by comparison with the vertical integral of $\varepsilon$ (Fig. 3f). The measured overturning circulation is found to principally extract energy from the lateral shear of the background flow, as expected from centrifugal instability, and to do so at rates of 0.1 – 0.5 W $m^{-2}$ that are broadly consistent with those of turbulent dissipation. Energy sources linked to gravitational and symmetric instabilities are generally negligible. Note that a close spatio-temporal correspondence between the energy source of centrifugal instability and turbulent dissipation is not expected, as centrifugal instability takes several hours to grow and generate the secondary instabilities that directly induce turbulent dissipation (see Supp. Info.).

In conclusion, our observations of the turbulent properties of the meltwater outflows from beneath the fast-melting PIIS show that centrifugal instability is a key contributor to the vigorous mixing that is responsible for the concentration of meltwater at the thermocline commonly documented across and beyond Pine Island

Bay[10-13]. The mechanism is triggered by the injection of high-buoyancy, meltwater-rich GMW at the PIIS calving front (Fig. 4). As GMW is more buoyant than the water above, it initially rises toward the upper ocean while undergoing gravitational instability, mixing and entraining ambient waters. This mixing and entrainment induce a localised vertical stretching and tilting of a density class slightly shallower than the ice shelf's base. The horizontal pressure gradient associated with the tilted density surfaces drives a geostrophic flow along the calving front that develops large anticyclonic relative vorticity in excess of the local planetary vorticity, and thus becomes unstable to centrifugal instability. This instability promotes an overturning circulation that transports GMW laterally away from the calving front and dilutes it rapidly through intense turbulent mixing, thereby arresting the meltwater's initial buoyant ascent.

This mechanism is reproduced by an idealised ocean circulation model configured with parameters and forcings appropriate to the PIIS outflow (see Supp. Info.). The model suggests that our observations provide a representative characterisation of the mechanism's dynamics, despite the measurements' omission, for reasons of navigational safety, of the initial gravitational instability adjacent to the base of the calving front. The model further indicates that the mechanism is likely to be of widespread relevance to buoyant meltwater outflows from beneath other Antarctic ice shelves, many of which are characterised by more modest melting rates[2,14]. Our findings thus show that the widely observed focussing of meltwater at depth is a dynamically robust feature of Antarctic ice sheet melting, and suggest that representation of the effects of centrifugal instability is critical to the realism of climate-scale ocean models with melting ice sheets. As explicit resolution of the mechanism (with respective horizontal and vertical scales of ~100 m and ~10 m; see

Supp. Info.) is presently beyond the capability of even regional models of ice shelf – ocean interaction[24,28], the development of a parameterisation of centrifugal instability of meltwater outflows from beneath floating ice shelves is called for.

## Methods

**PIIS calving front data set.** A set of targeted measurements of the hydrographic, velocity and shear microstructure properties of the ocean adjacent to the PIIS calving front was collected during expedition JR294/295 of the *RRS James Clark Ross* between 12 and 15 February 2014, supported by the *Ocean2ice* project of the U.K.'s Ice Sheet Stability programme (iSTAR, http://www.istar.ac.uk; see Fig. 1). The measurements were organised in three transects: two (transects S1A and S1B) directed parallel to and jointly spanning the PIIS calving front at a distance of 0.5 – 1 km from the front; and the other (transect S2) directed normally to the calving front along the main GMW outflow from the cavity at a distance of 0.5 – 4.5 km from the front. During each transect, a lightly-tethered, free-falling Rockland Scientific International VMP-2000 microstructure profiler was deployed continuously behind the slowly moving (at ~0.5 m $s^{-1}$) ship to acquire vertical profiles of measurements between approximately 10 m beneath the ocean surface and 100 m above the ocean floor. Temperature, salinity and pressure were measured on both down- and upcasts, whereas shear microstructure was solely recorded on downcasts, thereby yielding a reduced number of profiles and coarser inter-profile separation for microstructure measurements (70 profiles ~0.6 km apart, vs. 140 profiles ~0.3 km apart for hydrographic observations). Horizontal and vertical velocity measurements over the uppermost 600 m of the water column were obtained with a shipboard 75 kHz RD Instruments acoustic Doppler current profiler. The slow motion of the ship through the water and exceptionally calm sea state permitted the detection of significant vertical water velocities along transect S2 (Fig. 3c). Full details of the data set acquisition may be found in the JR294/95 cruise report, available online at https://www.bodc.ac.uk/data/information_and_inventories/cruise_inventory/report/jr294.pdf .

**Calculation of turbulent dissipation and mixing rates from microstructure measurements.** The rate of dissipation of turbulent kinetic energy, ε, was computed from microstructure measurements as $\varepsilon = 7.5\nu\overline{(\partial u'/\partial z)^2}$, where ν is the molecular viscosity and $\overline{(\partial u'/\partial z)^2}$ is the variance in the vertical shear of the horizontal velocity over the resolved turbulent wavenumber range[29]. Shear variance was calculated every 0.5 m, using shear spectra computed over a bin width of 1 s and integrated between 1 Hz and the spectral minimum in the 10 – 25 Hz band (or the 25 – 100 Hz band for $\varepsilon > 10^{-7}$ W kg$^{-1}$). The sampling rate of the vertical microstructure profiler was 512 Hz. The rate of turbulent diapycnal mixing, κ, was estimated from ε as $\kappa = \Gamma\,\varepsilon / N^2$, where Γ is a mixing efficiency (taken as 0.2 as pertinent to shear-driven turbulence) and $N$ is the buoyancy frequency[30].

**Calculation of potential vorticity.** The Ertel potential vorticity, $q$, is defined as $q = (f\hat{k} + \nabla \times \boldsymbol{u}) \cdot \nabla b$, where $f$ is the Coriolis parameter, $\hat{k}$ is the vertical unit vector, **u** is the three-dimensional velocity vector, and $b = -g\rho/\rho_0$ is the buoyancy ($g$ is the acceleration due to gravity, $\rho$ is density, and $\rho_0$ is a reference density)[25]. To calculate $q$ along transect S2 (Fig. 3e), we adopted the approximation $q \approx (f + \partial v/\partial x)N^2 - f|\partial \boldsymbol{u_h}/\partial z|^2$, where $\boldsymbol{u_h} = (u, v)$ is the horizontal velocity vector referenced to the along-transect ($u$) and across-transect ($v$) directions, and $x$ is the along-transect distance. This approximation is likely to underestimate the contribution of relative vorticity to $q$ (by less than a factor of 2), and assumes that the flow is in geostrophic balance to leading order. The validity of the approximation is assessed in the Supp. Info.

**Characterisation of overturning instabilities and their associated energy sources.** Overturning instabilities develop in areas where $fq < 0$ (refs. 25, 26). This criterion may be equivalently expressed as $\phi_{Ri_B} < \phi_c$ (ref. 26), where the balanced Richardson number angle $\phi_{Ri_B} = \tan^{-1}(-N^{-2}|\partial \boldsymbol{u_h}/\partial z|^2)$ and the critical angle $\phi_c = \tan^{-1}\left(-1 - f^{-1}\nabla \times \boldsymbol{u} \cdot \hat{k}\right) \approx \tan^{-1}(-1 - f^{-1}(\partial v/\partial x))$. The same assumptions as in the calculation of $q$ were adopted. When the instability criterion is met, the nature of the instability may be determined from the value of $\phi_{Ri_B}$ (ref. 27; Fig. 3e). Gravitational instability is associated with $-180° < \phi_{Ri_B} < -135°$ and $N^2 < 0$. Gravitational – symmetric instability corresponds to $-135° < \phi_{Ri_B} < -90°$ and $N^2 < 0$. Symmetric instability is indicated by $-90° < \phi_{Ri_B} < -45°$, with $N^2 > 0$ and $f^{-1}\nabla \times \boldsymbol{u} \cdot \hat{k} > 0$. Symmetric – centrifugal instability is implied by $-90° < \phi_{Ri_B} < -45°$, with $N^2 > 0$ and $f^{-1}\nabla \times \boldsymbol{u} \cdot \hat{k} < 0$. Centrifugal instability is linked to $\phi_{Ri_B} > -45°$, with $N^2 > 0$ and $f^{-1}\nabla \times \boldsymbol{u} \cdot \hat{k} < 0$.

Overturning instabilities derive their kinetic energy from a combination of convective available potential energy (gravitational instability), vertical shear production (symmetric instability) and lateral shear production (centrifugal instability)[27]. The rate of extraction of available potential energy along the S2 transect was estimated from measurements of the vertical velocity ($w$) and buoyancy as $F_b = \overline{w'b'}$, where the overline denotes a spatial average over the area of the instability and primes the deviation from that average. Here, the spatial average was computed horizontally at each depth level along the entire transect, to capture the buoyancy flux induced by the significant up- and downwelling flows associated with the instability (Fig. 3c). The rates of vertical and lateral shear production were estimated from velocity measurements as $P_{vrt} = -\overline{\boldsymbol{u_h}'w'} \cdot (\partial\overline{\boldsymbol{u_h}}/\partial z)$ and $P_{lat} = -\overline{\boldsymbol{u_h}'v_s'} \cdot (\partial\overline{\boldsymbol{u_h}}/\partial s)$, respectively, where $s$ is the horizontal coordinate perpendicular to the depth-integrated flow and $v_s$ is the component of $\boldsymbol{u_h}$in that direction. Here, the spatial average was calculated vertically at each horizontal location over the maximum common depth of the transect, to determine the momentum fluxes associated with the three-layered overturning flow (Fig. 3b).

## References

1. IPCC *Climate Change 2013: The Physical Science Basis* (eds Stocker, T. F. *et al.*) (Cambridge Univ. Press, 2014); http://www.climatechange2013.org/report/full-report

2. Shepherd, A. *et al.* A reconciled estimate of ice-sheet mass balance. *Science* **338**, 1183-1189 (2012).

3. Rye, C. D. *et al.* Rapid sea-level rise along the Antarctic margins in response to increased glacial discharge. *Nature Geosci.* **7**, 732-735 (2014).

4. Richardson, G., Wadley, M. R., Heywood, K. J., Stevens, D. P. & Banks, H. T. Short-term climate response to a freshwater pulse in the Southern Ocean. *Geophys. Res. Lett.* **32**, doi: 10.1029/2004GL021586 (2005).

5. Bintanja, R., van Oldenborgh, G. H., Drijfhout, S. S., Wouters, B. & Catsman, C. A. Important role for ocean warming and increased ice-shelf melt in Antarctic sea-ice expansion. *Nature Geosci.* **6**, 376-379 (2013).

6. Purkey, S. G. & Johnson, G. C. Global contraction of Antarctic Bottom Water between the 1980s and 2000s. *J. Clim.* **25**, 5830-5844 (2012).

7. Arrigo, K. R., van Dijken, G. L. & Strong, A. L. Environmental controls of marine productivity hot spots around Antarctica. *J. Geophys. Res.* **120**, 5545-5565 (2015).

8. Arrigo, K. R., van Dijken, G. & Long, M. Coastal Southern Ocean: A strong anthropogenic $CO_2$ sink. *Geophys. Res. Lett.* **35**, doi: 10.1029/2008GL035624 (2008).

9. Swart, N. C. & Fyfe, J. C. The influence of recent Antarctic ice sheet retreat on simulated sea ice area trends. *Geophys. Res. Lett.* **40**, doi:10.1002/grl.50820 (2013).

10. Dutrieux, P. *et al.* Strong sensitivity of Pine Island Ice-Shelf melting to climatic variability. *Science* **343**, 174-178 (2014).

11. Hohmann, R., Schlosser, P., Jacobs, S., Ludin, A. & Weppernig, R. Excess helium and neon in the southeast Pacific: tracers for glacial meltwater. *J. Geophys. Res.* **107**, doi:10.1029/2000JC000378 (2002).

12. Loose, B., Schlosser, P., Smethie, W. M. & Jacobs, S. An optimized estimate of glacial melt from the Ross Ice Shelf using noble gases, stable isotopes, and CFC transient tracers. *J. Geophys. Res.* **114**, doi:10.1029/2008JC005048 (2009).

13. Nicholls, K. W., Østerhus, S., Makinson, K., Gammelsrød, T. & Fahrbach, E. Ice-ocean processes over the continental shelf of the southern Weddell Sea, Antarctica: A review. *Rev. Geophys.* **47**, doi: 10.1029/2007RG000250 (2009).

14. Kim, I. *et al.* The distribution of glacial meltwater in the Amundsen Sea, Antarctica, revealed by dissolved helium and neon. *J. Geophys. Res.*, doi:10.1002/2015JC011211 (2016).

15. Paolo, F. S., Fricker, H. A. & Padman, L. Volume loss from Antarctic ice shelves is accelerating. *Science* **348**, 327-331 (2015).

16. Feldmann, J. & Levermann, A. Collapse of the West Antarctic Ice Sheet after local destabilization of the Amundsen Basin. *Proc. Natl. Aca. Sci.* **112**, 14191-14196 (2015).

17. Pritchard, H. D. *et al.* Antarctic ice-sheet loss driven by basal melting of ice shelves. *Nature* **484**, 502-505 (2012).

18. Joughin, I., Alley, R. B. & Holland, D. M. Ice-sheet response to oceanic forcing. *Science* **338**, 1172-1176 (2012).

19. Thoma, M., Jenkins, A. Holland, D. & Jacobs, S. Modelling Circumpolar Deep Water intrusions on the Amundsen Sea continental shelf, Antarctica. *Geophys. Res. Lett.* **35**, doi:10.1029/2008GL034939 (2008).

20. Stewart, A. L. & Thompson, A. F. Eddy-mediated transport of warm Circumpolar Deep Water across the Antarctic shelf break. *Geophys. Res. Lett.* **42**, 432-440 (2015).

21. Schmidtko, S., Heywood, K. J., Thompson, A. F. & Aoki, S. Multidecadal warming of Antarctic waters. *Science* **346**, 1227-1231 (2014).

22. Pauling, A. G., Bitz, C. M., Smith, I. J. & Langhorne, P. J. The response of the Southern Ocean and Antarctic sea ice to freshwater from ice shelves in an Earth system model. *J. Clim.* **29**, 1655-1672.

23. Thurnherr, A. M., Jacobs, S. S., Dutrieux, P. & Giulivi, C. F. Export and circulation of ice cavity water in Pine Island Bay, West Antarctica. *J. Geophys. Res.* **119**, 1754-1764 (2014).

24. St. Laurent, P., Klinck, J. & Dinniman, M. Impact of local winter cooling on the

melt of Pine Island Glacier, Antarctica. *J. Geophys. Res.* **120**, doi:10.1002/2015jc010709 (2015).

25. Hoskins, B. J. The role of potential vorticity in symmetric stability and instability. *Quart. J. Roy. Met. Soc.* **100**, 480-482 (1974).

26. Haine, T. W. N. & Marshall, J. Gravitational, symmetric, and baroclinic instability of the ocean mixed layer. *J. Phys. Oceanogr.* **28**, 634-658 (1998).

27. Thomas, L. N., Taylor, J. R., Ferrari, R. & Joyce, T. M. Symmetric instability in the Gulf Stream. *Deep-Sea Res. II* **91**, 96-110 (2013).

28. Nakayama, Y., Timmermann, R., Rodehacke, C. B., Schröder, M. & Hellmer, H. H. Modeling the spreading of glacial meltwater from the Amundsen and Bellingshausen Seas. *Geophys. Res. Lett.* **41**, doi:10.1002/2014GL061600 (2014).

29. Oakey, N. S. Determination of the rate of dissipation of turbulent energy from simultaneous temperature and velocity shear microstructure measurements. *J. Phys. Oceanogr.* **12**, 256-271 (1982).

30. Osborn, T. R. Estimates of the local rate of vertical diffusion from dissipation measurements. *J. Phys. Oceanogr.* **10**, 83-89 (1980).

**Supplementary information** is linked to the online version of the paper at www.nature.com/nature

**Acknowledgements** The iSTAR programme is supported by the Natural Environment Research Council of the U.K. (grant NE/J005703/1). A.C.N.G. acknowledges the support of a Philip Leverhulme Prize, the Royal Society, and the Wolfson Foundation. We are grateful to the scientific party, crew and technicians on the *RRS James Clark Ross* for their hard work during data collection.

**Author Contributions** A.C.N.G. and A.F. designed and conducted the data analysis, with contributions from P.D. and L.C.B. L.B. designed and conducted the idealised model experiments. K.J.H. led the JR294/295 research cruise. All authors contributed to the scientific interpretation of the results.

**Author Information** Reprints and permissions information is available at www.nature.com/reprints. Correspondence and requests for materials should be addressed to acng@noc.soton.ac.uk

## Figure legends

**Figure 1 | Map of the study region.** Positions of hydrographic / microstructure profiles are shown by circles, coloured by the mean meltwater content (ml $l^{-1}$) in the 100 – 700 m depth range estimated as in ref. (10). Horizontal velocity (gridded in 3 km × 3 km bins) in the upper ocean (0 – 300 m) measured with a ship-mounted acoustic Doppler current profiler is indicated by white vectors, with black vectors showing measurements in January 2009 (ref. 23). Seabed elevation (m) is denoted by blue shading, ice photography (TERRA image from 27 January 27 2014) by grey shading, and ice shelf / ice sheet boundaries by white lines. Transects S1A, S1B and S2 are labelled. The red rectangle marks the position of a mooring used in assessing the significance of tidal flows (see Supp. Info.).

**Figure 2 | Transect along the PIIS calving front**. (a) Potential temperature ($\theta$, colour) and neutral density (in kg $m^{-3}$, black contours), with positions of stations indicated by grey tick marks at the base of the figure. (b) Across-transect velocity ($v$), with positive values directed northwestward (out of the PIIS cavity). (c) Rate of turbulent kinetic energy dissipation ($\varepsilon$, a metric of the intensity of small-scale turbulence, in colour), with contours of meltwater concentration (see Supp. Info.) superimposed. (d) Rate of diapycnal mixing ($\kappa$, colour), with contours as in (c). Both $\varepsilon$ and $\kappa$ are calculated from microstructure measurements (see Methods). Distance is measured from the origin of the S1A transect, at the southwestern corner of the PIIS calving front. The break point near 30 km indicates the transition from the S1A transect to the S1B transect. The characteristic vertical extent of the PIIS is shown by the grey rectangle at the right-hand axis of each panel.

**Figure 3 | Transect along the main outflow from the PIIS calving front.** (a) Potential temperature (θ, colour), neutral density (in kg $m^{-3}$, black contours) and mixed layer depth (determined from the maximum in buoyancy frequency, dashed white contour), with positions of stations indicated by grey tick marks on the upper axis. (b) Along-transect velocity ($u$, colour), with positive values directed southeastward (into the PIIS cavity). (c) Vertical velocity ($w$, colour), with positive values directed upward. (d) Rate of turbulent kinetic energy dissipation (ε, colour). Potential temperature contours are shown at intervals of 0.2°C in (b)-(d). (e) Potential vorticity ($q$, colour). Areas of positive $q$ (indicative of overturning instabilities) are outlined. The outline shading denotes the instability type (GRV = gravitational; SYM = symmetric; CTF = centrifugal; see Methods). The characteristic vertical extent of the PIIS is shown by the grey rectangle at the right-hand axis of (a)-(e). f) Comparison between the vertically integrated (between depths of 50 m, below the base of the upper-ocean mixed layer, and 610 m, the maximum common depth of the transect) rates of turbulent kinetic energy dissipation (ε) and of turbulent kinetic energy production associated with gravitational instability ($F_b$), symmetric instability ($P_{vrt}$) and centrifugal instability ($P_{lat}$). See Methods.

**Figure 4 | Schematic of the meltwater outflow from beneath the PIIS.** The direction of flow is indicated by the thick arrows, surfaces of constant density are denoted by solid white contours, and the upper-ocean mixed layer base is marked by the dashed white line. The direction of the along-calving-front flow is shown by the circle, and the sense of rotation of the meltwater plume as it is about to experience centrifugal instability is indicated in the upper axis ($\zeta$ = relative vorticity; f = planetary vorticity).

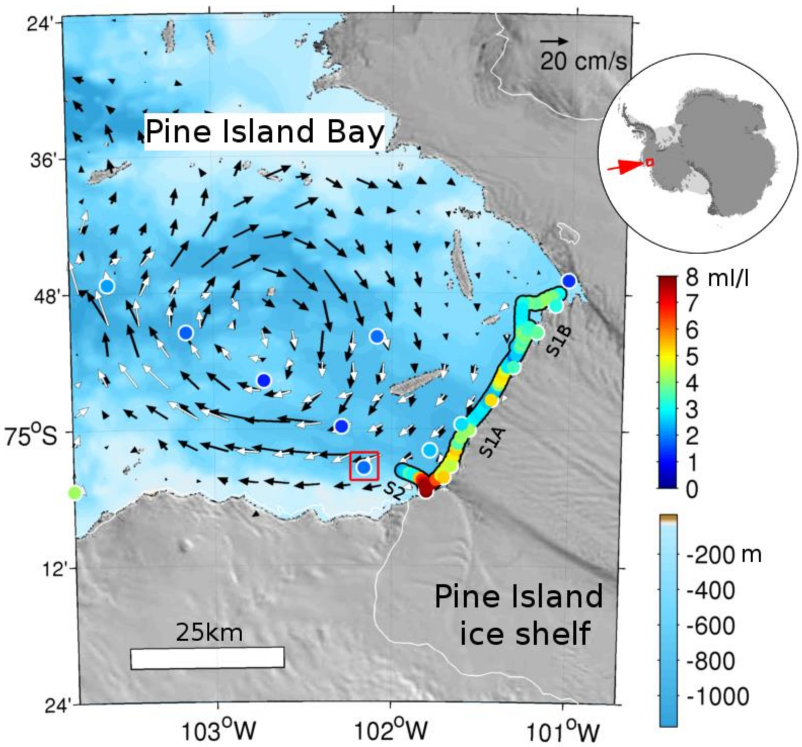


**Figure 1 | Map of the study region.** Positions of hydrographic / microstructure profiles are shown by circles, coloured by the mean meltwater content (ml $l^{-1}$) in the 100 – 700 m depth range estimated as in ref. (10). Horizontal velocity (gridded in 3 km × 3 km bins) in the upper ocean (0 – 300 m) measured with a ship-mounted acoustic Doppler current profiler is indicated by white vectors, with black vectors showing measurements in January 2009 (ref. 23). Seabed elevation (m) is denoted by blue shading, ice photography (TERRA image from 27 January 27 2014) by grey shading, and ice shelf / ice sheet boundaries by white lines. Transects S1A, S1B and S2 are labelled. The red rectangle marks the position of a mooring used in assessing the significance of tidal flows (see Supp. Info.).

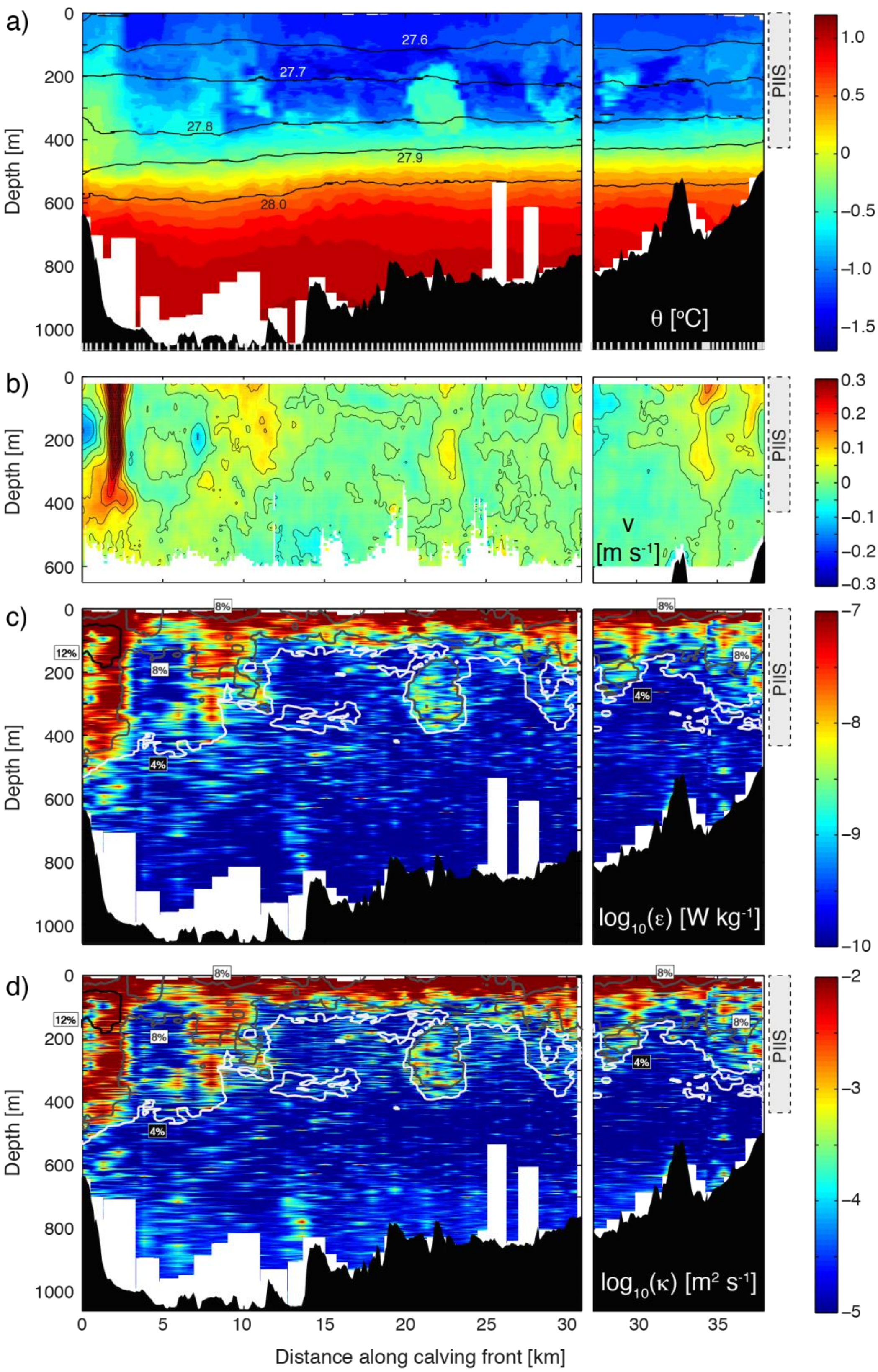


**Figure 2 | Transect along the PIIS calving front**. (a) Potential temperature (θ, colour) and neutral density (in kg m$^{-3}$, black contours), with positions of stations indicated by grey tick marks at the base of the figure. (b) Across-transect velocity (*v*), with positive values directed northwestward (out of the PIIS cavity). (c) Rate of turbulent kinetic energy dissipation (ε, a metric of the intensity of small-scale turbulence, in colour), with contours of meltwater concentration (see Supp. Info.) superimposed. (d) Rate of diapycnal mixing (κ, colour), with contours as in (c). Both ε and κ are calculated from microstructure measurements (see Methods). Distance is measured from the origin of the S1A transect, at the southwestern corner of the PIIS calving front. The break point near 30 km indicates the transition from the S1A transect to the S1B transect. The characteristic vertical extent of the PIIS is shown by the grey rectangle at the right-hand axis of each panel.

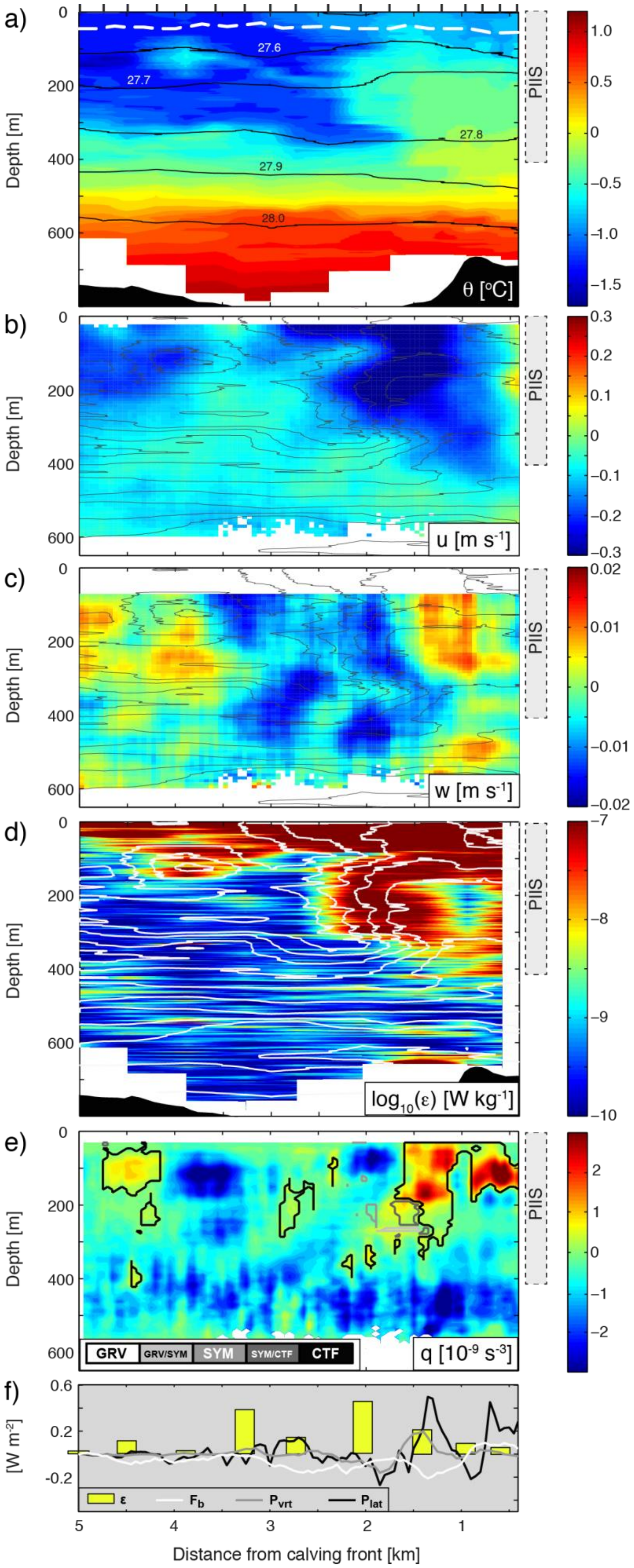

a)
b)
c)
d)
e)
f)
Depth [m]
PIIS
27.6
27.7
27.8
27.9
28.0
θ [°C]
u [m s-1]
w [m s-1]
log10(ε) [W kg-1]
q [10-9 s-3]
GRV
GRV/SYM
SYM
SYM/CTF
CTF
[W m-2]
ε
Fb
Pvrt
Plat
Distance from calving front [km]


459

**Figure 3 | Transect along the main outflow from the PIIS calving front.** (a) Potential temperature (θ, colour), neutral density (in kg $m^{-3}$, black contours) and mixed layer depth (determined from the maximum in buoyancy frequency, dashed white contour), with positions of stations indicated by grey tick marks on the upper axis. (b) Along-transect velocity ($u$, colour), with positive values directed southeastward (into the PIIS cavity). (c) Vertical velocity ($w$, colour), with positive values directed upward. (d) Rate of turbulent kinetic energy dissipation (ε, colour). Potential temperature contours are shown at intervals of 0.2°C in (b)-(d). (e) Potential vorticity ($q$, colour). Areas of positive $q$ (indicative of overturning instabilities) are outlined. The outline shading denotes the instability type (GRV = gravitational; SYM = symmetric; CTF = centrifugal; see Methods). The characteristic vertical extent of the PIIS is shown by the grey rectangle at the right-hand axis of (a)-(e). f) Comparison between the vertically integrated (between depths of 50 m, below the base of the upper-ocean mixed layer, and 610 m, the maximum common depth of the transect) rates of turbulent kinetic energy dissipation (ε) and of turbulent kinetic energy production associated with gravitational instability ($F_b$), symmetric instability ($P_{vrt}$) and centrifugal instability ($P_{lat}$). See Methods.

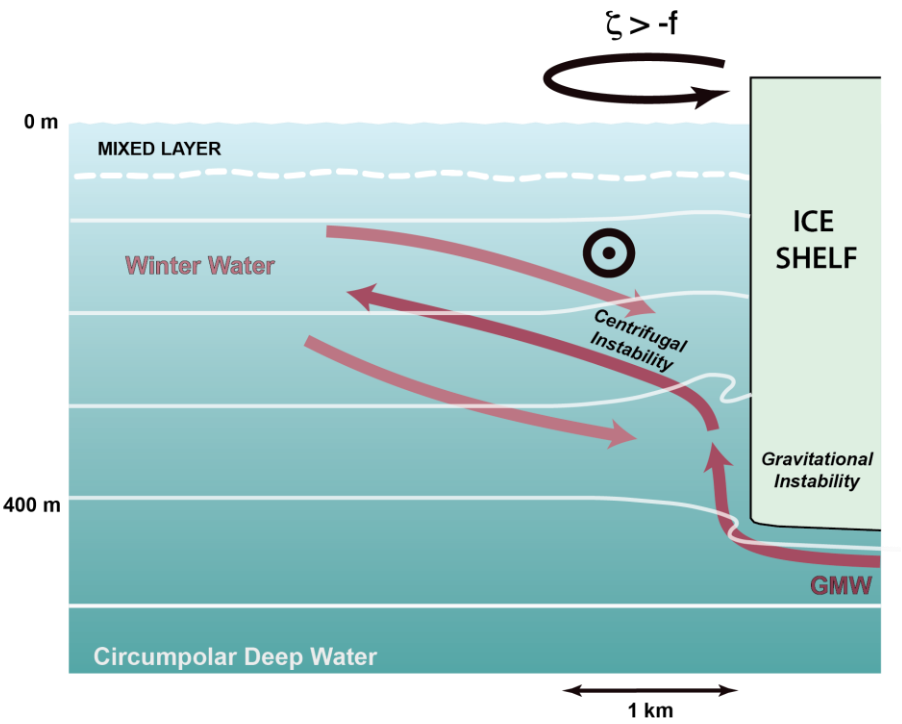


**Figure 4 | Schematic of the meltwater outflow from beneath the PIIS.** The direction of flow is indicated by the thick arrows, surfaces of constant density are denoted by solid white contours, and the upper-ocean mixed layer base is marked by the dashed white line. The direction of the along-calving-front flow is shown by the circle, and the sense of rotation of the meltwater plume as it is about to experience centrifugal instability is indicated in the upper axis ($\zeta$ = relative vorticity; $f$ = planetary vorticity).